Developing high-impedance superconducting resonators and on-chip filters for semiconductor quantum dot circuit quantum electrodynamics

X. Zhang, ¹ Z. Zhu, ¹ N. P. Ong, ¹ and J. R. Petta^{2,3}

¹Department of Physics, Princeton University, Princeton, New Jersey 08544, USA

²Department of Physics and Astronomy, University of California – Los Angeles, Los Angeles, California 90095, USA

³Center for Quantum Science and Engineering, University of California – Los Angeles, Los Angeles, California 90095, USA

Spin-photon coupling presents an enticing opportunity for the long-range coupling of spin qubits. The spin-photon coupling rate g_s is proportional to the charge-photon coupling rate g_c . To move deeper into the strong coupling regime, g_c can be enhanced by fabricating high-impedance cavities using high kinetic inductance films. Here we report dc transport and microwave response investigations of niobium nitride (NbN) films of different thicknesses. The kinetic inductance increases rapidly as the film thickness is reduced below 50 nm and for 15 nm NbN films we measure a sheet kinetic inductance $L_{k,S} = 41.2 \text{ pH/}\square$. As an application of the high kinetic inductance films, we fabricate compact LC filters that are commonly used to reduce microwave leakage in circuit quantum electrodynamics (cQED) devices. These filters feature up to 60 dB of attenuation near typical cavity resonance frequencies $f_c = 8 \text{ GHz}$.

I. INTRODUCTION

In recent years, quantum computing has been a field of fast-growing interest and intense research. In the quest for a large-scale quantum computing architecture, individual processing units can be interconnected via a coherent mediator, allowing entanglement to be spread across the quantum circuit. Many different schemes for short-range nearest-neighbor entanglement have been demonstrated and perfected [1–4]. However, long-range coupling between distant qubits has remained a challenge. To date, some approaches to achieve long-range qubit entanglement include coherently shuttling electrons using gate-voltage pulses [5, 6] or surface acoustic waves [7–10], coupling spin qubits with a much larger coupling quantum dot (QD) [11], or using a microwave cavity as a mediator [12–16].

Strong spin-photon coupling has been achieved in circuit quantum electrodynamics (cQED) device architectures by isolating a single electron in a Si double quantum dot (DQD) and utilizing the field gradient from a nearby micromagnet to engineer a synthetic spin-orbit interaction [12, 13]. Exchange-only spin qubits fabricated in GaAs have also reached the strong coupling regime [14]. Resonant coupling of two spin qubits separated by \sim 4 mm has been demonstrated [15] and attempts have been made to extend cavity-mediated spin-spin coupling into the dispersive regime [17]. However, a larger spin-photon coupling rate g_s is needed to achieve high-fidelity remote gates between spatially separated spins.

The spin-photon coupling rate is set by the electric dipole moment of the electron trapped in the DQD, the cavity electric field, and the strength of the effective spin-orbit interaction. The cavity field is a function of the characteristic impedance of the resonator Z_C . Therefore, an enhancement in g_s can be achieved by increasing Z_C , as $g_s \propto g_c \propto \sqrt{Z_C}$. The kinetic inductance can be greatly increased using large arrays of superconducting quantum interference devices (SQUIDs) [18]. However, for single spin qubits, the magnetic fields required to Zeeman split the spin states interferes with the operation of SQUID arrays.

Another way to increase characteristic impedance of the

resonator is to fabricate it from a high kinetic inductance superconducting film. The resonator impedance is given by $Z_C = \sqrt{\frac{L}{C}}$, where L and C are the characteristic inductance and capacitance. The inductance $L = L_m + L_k$, can be separated into magnetic, L_m , and kinetic, L_k , components. In past experiments, the magnetic inductance has been modestly increased using narrow Nb stripline resonators with an estimated impedance $Z_C \sim 300 \Omega$ [12]. For some superconducting materials, L_k is dominant compared with L_m [19]. Therefore, to tune Z_C to a greater extent, high kinetic inductance materials are desirable. Since L_k is directly proportional to the ratio of the resonator length l to the cross-sectional area of the superconducting film [20], an effective approach is to fabricate a narrow resonator from a thin film of a high L_k material [17, 21].

In this Article, we study high L_k NbN thin films and present two different approaches for extracting the sheet kinetic inductance $L_{k,S}$. We begin with dc resistivity measurements across the superconducting transition and compute $L_{k,S}$ over a large range of film thicknesses. We next characterize the microwave response of quarter-wavelength ($\lambda/4$) hanger-style resonators fabricated from NbN. To investigate the thickness dependence of $L_{k,S}$, we measure a variety of resonators, and from the extracted resonance frequencies we determine the kinetic inductance contribution to the total inductance. The kinetic inductance values $L_{k,S}$ extracted from dc and microwave measurements are in good agreement. Lastly, we utilize thin NbN films to fabricate compact LC filters that are compatible with QD-cQED devices. These filters feature up to 60 dB of attenuation near typical cavity resonance frequencies $f_c = 8$ GHz and have a footprint that is significantly smaller than our previous design [12].

II. NIOBIUM NITRIDE FILM DEPOSITION AND DC RESISTIVITY MEASUREMENTS

We begin by characterizing the sheet resistance and critical temperature T_C of unpatterned superconducting NbN thin films using dc transport measurements. From the Bardeen-

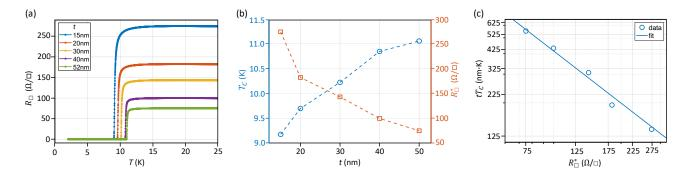


FIG. 1. (a) Temperature dependence of the sheet resistance R_{\square} for NbN thin films of different thicknesses t measured near the superconducting transition. (b) Critical temperature $T_{\rm C}$ and normal state sheet resistance R_{\square}^* as a function of t. The dashed lines are guides to the eye. (c) $tT_{\rm C}$ plotted as a function of R_{\square}^* . The blue solid line is a fit to the universal scaling relation $tT_{\rm C} = AR_{\square}^{*-b}$, yielding the power-law exponent $b = 1.1 \pm 0.3$.

Cooper-Schrieffer (BCS) theory of superconductivity, these quantities can be used to estimate the kinetic inductance [19, 22].

We use an AJA dc-magnetron sputtering system with a high-purity Nb target to deposit the NbN films. Taking the critical temperature T_C as a metric, we optimize the deposition parameters, including gas flow rates, target power, and deposition pressure. With a base pressure below 2×10^{-9} Torr, we initiate the deposition process by introducing N_2 and Ar into the system at flow rates of 6 sccm and 60 sccm to condition the chamber. We then bias the Nb target with a power of 400 W to ignite a plasma. The plasma of ions dislodges Nb atoms from the target, and the Nb atoms react with N_2 to form NbN, which then deposits onto the substrate. The chamber pressure is held at 10 mTorr during deposition. We deposited five NbN thin films of various thicknesses, with the substrate held at room temperature, utilizing a deposition rate of approximately 12 Å/s.

The thin films are characterized in a physical property measurement system (PPMS). We measure the sheet resistance R_{\square} as a function of temperature T using conventional 4-probe transport techniques. As shown in Fig. 1(a), all films exhibit sharp superconducting transitions below T = 12 K. From each cooldown curve, we extract the superconducting critical temperature T_C and the normal state sheet resistance just before the superconducting transition R_{\square}^* . T_C is defined as the temperature at which R_{\square} drops to half of its normal state value. T_C and R_{\square}^* are plotted as a function of film thickness t in Fig. 1(b). As the film thickness t decreases, R_{\square}^* increases, while T_C monotonically decreases. The general trends observed in the temperature dependence of T_C and R_{\square}^* are in agreement with prior work [23–25]. In Fig. 1(c), we plot tT_C as a function of R_{\square}^* . The data are fit to the scaling relation $tT_C = AR_{\square}^{*-b}$ [26]. We extract the exponent $b = 1.1 \pm 0.3$, which agrees with $b \approx 0.9 \sim 1.1$ widely observed in highquality superconducting thin films [26–28].

Using the extracted T_C and R_{\square}^* , we estimate the sheet kinetic inductance using the formula [19]

$$L_{k,S} = \frac{\hbar R_{\square}^*}{\pi \Delta_0},\tag{1}$$

t (nm)	$T_{C}\left(\mathbf{K}\right)$	$R_{\square}^{*}\left(\Omega/\square ight)$	$L_{k,S}\left(\mathrm{pH}/\Box\right)$
15	9.2	273.9	41.2
20	9.7	182.1	25.9
30	10.2	143.2	19.3
40	10.8	99.8	12.7
52	11.1	75.1	9.4

TABLE I. Critical temperature T_C , normal state sheet resistance R_{\square}^* , and sheet kinetic inductance $L_{k,S}$ for various film thicknesses t.

where \hbar is the reduced Planck's constant and Δ_0 is the zero temperature superconducting gap. Assuming the NbN thin films obey BCS theory, $\Delta_0 = 1.76 \times k_B T_C$, where k_B is Boltzmann's constant [22]. The extracted values of T_C , R_\square^* , and the evaluated results of $L_{k,S}$, are given in Table I. As t decreases from 52 nm to 15 nm, we observe a large increase in R_\square^* from 75.1 Ω/\square to 273.9 Ω/\square and a small decrease in T_C from 11.1 K to 9.2 K, resulting in a significant increase in $L_{k,S}$ from 9.4 pH/ \square to 41.2 pH/ \square . These estimated kinetic inductance values allow for the efficient design of microwave cavities.

III. MICROWAVE RESONATOR CHARACTERIZATION OF THE KINETIC INDUCTANCE

Using the kinetic inductance values obtained in Sec. II, we design microwave cavities with resonance frequencies ranging from 5.8-6.4 GHz. We fabricate an array of $\lambda/4$ cavities that are coupled to a transmission line. The side-coupled cavities allow for the efficient extraction of resonance frequencies and quality factors [20, 29]. By fabricating resonators with different dimensions, we can quantitatively extract the magnetic and kinetic contributions to the total inductance.

As shown in Fig. 2(a), a typical resonator chip contains $12 \lambda/4$ resonators of varying length l, each capacitively coupled to a central transmission line. The sample is made from a 30 nm NbN thin film sputtered on a high-resistivity Si substrate, and the resonators are of the coplanar waveguide (CPW) design with a central conductor width $a = 10 \mu m$ and

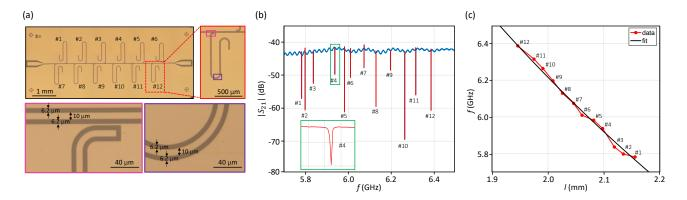


FIG. 2. Microwave characterization of hanger-style resonators. (a) Optical images of samples containing $12 \lambda/4$ resonators of varying length l that are coupled to a central transmission line. Insets: Zoomed-in images showing resonator dimensions. (b) Microwave transmission $|S_{21}(f)|$ through a sample made from a 30 nm NbN film. The 12 resonances are highlighted in red. Inset: Zoom-in of $|S_{21}(f)|$ near the resonance at f = 5.9 GHz. (c) Extracted resonance frequencies plotted as a function of l, showing the expected 1/l dependence. A linear fit to the data (solid line) using a transmission line model yields a sheet kinetic inductance $L_{k,S} = 20.9 \text{ pH/}\square$.

a gap width $s = 6.2 \ \mu m$. We use a network analyzer to characterize the microwave response of the sample, $|S_{21}(f)|$, in a dilution refrigerator with a lattice temperature of approximately 10 mK. Each resonance results in a Lorentzian dip in $|S_{21}(f)|$. In Fig. 2(b), 12 resonances are observed (highlighted in red), corresponding to the 12 different resonator lengths.

In Fig. 2(c), we plot the extracted resonance frequencies of all 12 resonators and observe the expected relationship $f \propto 1/l$. For a $\lambda/4$ resonator, the resonator length can be written as

$$l = \lambda/4 = \frac{v_{\text{eff}}}{4f_0},\tag{2}$$

where λ is the wavelength and f_0 is the resonance frequency. For non-magnetic substrates, the propagation speed is $v_{\rm eff} = \frac{c}{\sqrt{\mu_{\rm eff} \varepsilon_{\rm eff}}} \approx \frac{c}{\sqrt{\varepsilon_{\rm eff}}}$, where c is the speed of light in vacuum, $\mu_{\rm eff}$ is the relative magnetic permeability, and $\varepsilon_{\rm eff}$ is the relative dielectric constant, defined as

$$\varepsilon_{\text{eff}} = \frac{1 + \varepsilon_r \tilde{K}}{1 + \tilde{K}}.$$
 (3)

The value of $\varepsilon_{\rm eff}$ is determined by the geometry of the CPW resonator and the relative dielectric constant of the substrate $\varepsilon_r = 11.7$, with \tilde{K} given by

$$\tilde{K} = \frac{K(k')K(k_3)}{K(k)K(k_3')}. (4)$$

Here *K* is the complete elliptical integral of the first kind, with $k = \frac{a}{b}$, $k_3 = \frac{\tanh(\frac{\pi a}{4h})}{\tanh(\frac{\pi b}{4h})}$, $k' = \sqrt{1 - k^2}$, $k'_3 = \sqrt{1 - k_3^2}$, and b = a + 2s, where *a* is the center conductor width, *s* is the gap width, and *h* is the substrate thickness [30, 31].

In a CPW geometry, the magnetic inductance per unit length is given by [29]:

$$L_m = \frac{\mu}{4} \frac{K(k')}{K(k)},\tag{5}$$

where μ is the magnetic permeability of the substrate. In the case of a high- L_k resonator, the kinetic inductance must be included to obtain the total inductance, $L = L_m + L_k$. With $f \propto 1/\sqrt{L}$, we can fit to the data to extract $L_{k,S} = 20.9$ pH/ \square [solid line in Fig. 2(c)], which is close to the estimate obtained from the PPMS data. As the magnetic inductance only depends on the CPW geometry, we use the resonator dimensions to calculate the sheet magnetic inductance $L_{m,S} = 4.4$ pH/ \square .

To investigate the thickness dependence of $L_{k,S}$, we fabricate a variety of hanger-style resonators using NbN thin films of different thicknesses. For each film thickness, we determine $L_{k,S}$ by fitting to the measured resonance frequencies, as described in the previous paragraph. Figure 3 combines results from dc resistivity measurements and microwave resonator characterization. The values of $L_{k,S}$ extracted from microwave measurements are in good agreement with the estimates obtained from dc transport measurements. The kinetic inductance of the NbN films is significant. For a direct comparison, the kinetic inductance extracted from a set of resonators fabricated on a conventional 50 nm thick Nb film is only $L_{k,S} = 0.5$ pH/ \square .

As expected from theory, $L_{k,S}$ rapidly increases as t is reduced below 50 nm, with the highest value $L_{k,S} = 58.7 \text{ pH/}\square$ obtained from hanger resonators made from a 12.5 nm film. Our past cQED devices utilized 50 nm Nb films and the largest coupling rates measured were $g_c \approx 58$ MHz in Ref. [16] and $g_{c(s)} \approx 40$ (11) MHz in Ref. [15]. To estimate the potential enhancement in $g_{c(s)}$ by switching to 15 nm NbN with $L_{k,S} = 41.2 \text{ pH/}\square$, we compare the total inductances assuming the same $\lambda/2$ resonator design using the two different materials. The $\lambda/2$ resonators on our current QD-cQED chips have a center pin width $a = 0.75 \ \mu\text{m}$ and gap width $s = 19.63 \ \mu\text{m}$, which yields a sheet magnetic inductance $L_{m,S} = 0.85 \ \text{pH/}\square$. With 15 nm NbN thick films, the magnetic inductance is only 2% of the total inductance. Since $g_{c(s)} \propto \sqrt{Z_C} \propto L^{1/4}$, switching from 50 nm Nb to 15 nm NbN is expected to result in a 5.6× increase in Z_C , and hence a 2.4× increase in $g_{c(s)}$.

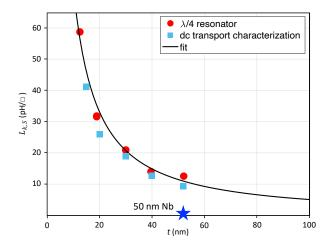


FIG. 3. Thickness dependence of the sheet kinetic inductance $L_{k,S}$. The data are extracted from the dc characterization of the thin film resistivity (Sec. II) and the microwave response of $\lambda/4$ resonators (Sec. III). The blue star indicates the much smaller $L_{k,S} = 0.5 \text{ pH/}\Box$ of a standard 50 nm Nb film.

IV. LC MICROWAVE FILTERS FOR QUANTUM DOT CIRCUIT QUANTUM ELECTRODYNAMICS

We now utilize high kinetic inductance NbN films to fabricate compact microwave filters. Measurements of early QDcQED devices show significant microwave leakage through the wiring used to dc bias the QD gate electrodes [32]. The resulting photon leakage pathways can lower the cavity quality factor significantly. To suppress photon leakage, on-chip lowpass LC filters are often connected in series with each gate line [33]. Each LC filter consists of a spiral inductor and an interdigitated capacitor (see Fig. 4 insets). We simulate different designs using the Sonnet EM simulation package and fabricate Nb and NbN filters to evaluate their performance.

Figure 4 shows the microwave transmission $|S_{21}(f)|$ through two types of filters that are cooled to $T \sim 700$ mK. The filter fabricated from a standard 50 nm thick Nb film provides \sim 24 dB of attenuation near a typical cavity frequency of 8 GHz [33]. In contrast, a filter fabricated using a 15 nm thick NbN film is approximately $2\times$ shorter and provides a much larger attenuation of 60 dB near 8 GHz. The experimental data are in good agreement with Sonnet simulations. These measurements show that the utilization of NbN films can significantly reduce filter sizes and provide a higher degree of attenuation to reduce cavity losses.

V. CONCLUSION

In summary, we have investigated the thickness dependence of the sheet kinetic inductance of sputtered NbN thin films using a combination of dc transport and microwave measurements. To mitigate microwave leakage through the QD dc gate lines, we tested different LC filter designs and demon-

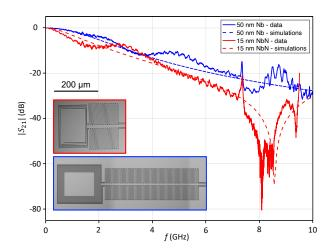


FIG. 4. Measurements of $|S_{21}(f)|$ for two LC filters (solid lines) and the simulated response (dashed lines). The 15 nm NbN filter (red) gives a substantial attenuation of 60 dB around 8 GHz. In comparison, we measure 24 dB of attenuation using a \sim 2× longer filter made from a 50 nm Nb film (blue). Insets: Optical images of filters fabricated from a 15 nm NbN film (outlined in red) and a 50 nm Nb film (outlined in blue).

strated 60 dB of attenuation near typical cavity resonance frequencies. Owing to the high L_k of NbN, we can now achieve much stronger on-chip filtering with a smaller filter footprint. The high kinetic inductance $L_{k,S} = 41.2 \text{ pH/}\square$ of the 15 nm NbN film provides an opportunity to further enhance g_c and g_s , thereby moving QD-cQED systems further into the strong coupling regime.

ACKNOWLEDGMENTS

Supported by Army Research Office grants W911NF-15-1-0149 and W911NF-23-1-0104. Devices were fabricated in the Princeton University Quantum Device Nanofabrication Laboratory, and in part in the Singh Center for Nanotechnology, which is supported by the NSF National Nanotechnology Coordinated Infrastructure Program under grant NNCI-2025608. NPO acknowledges support from the U.S. Department of Energy (DE-SC0017863).

- [1] J. R. Petta, A. C. Johnson, J. M. Taylor, E. A. Laird, A. Yacoby, M. D. Lukin, C. M. Marcus, M. P. Hanson, and A. C. Gossard, Coherent manipulation of coupled electron spins in semiconductor quantum dots, Science 309, 2180 (2005).
- [2] P.-A. Mortemousque, E. Chanrion, B. Jadot, H. Flentje, A. Ludwig, A. D. Wieck, M. Urdampilleta, C. Bäuerle, and T. Meunier, Coherent control of individual electron spins in a two-dimensional quantum dot array, Nat. Nanotechnol. 16, 296 (2021).
- [3] T. Watson, S. Philips, E. Kawakami, D. Ward, P. Scarlino, M. Veldhorst, D. Savage, M. Lagally, M. Friesen, S. Coppersmith, et al., A programmable two-qubit quantum processor in silicon, Nature 555, 633 (2018).
- [4] D. Zajac, A. Sigillito, M. Russ, F. Borjans, J. Taylor, G. Burkard, and J. Petta, Resonantly driven CNOT gate for electron spins, Science 359, 439 (2018).
- [5] T. A. Baart, M. Shafiei, T. Fujita, C. Reichl, W. Wegscheider, and L. M. K. Vandersypen, Single-spin charge-coupled device, Nat. Nanotechnol. 11, 330 (2016).
- [6] A. Mills, D. Zajac, M. Gullans, F. Schupp, T. Hazard, and J. Petta, Shuttling a single charge across a one-dimensional array of silicon quantum dots, Nat. Commun. 10, 1 (2019).
- [7] M. M. de Lima and P. V. Santos, Modulation of photonic structures by surface acoustic waves, Rep. Prog. Phys. 68, 1639 (2005)
- [8] J. A. Stotz, R. Hey, P. V. Santos, and K. H. Ploog, Coherent spin transport through dynamic quantum dots, Nat. Mater. 4, 585 (2005).
- [9] S. Hermelin, S. Takada, M. Yamamoto, S. Tarucha, A. D. Wieck, L. Saminadayar, C. Bäuerle, and T. Meunier, Electrons surfing on a sound wave as a platform for quantum optics with flying electrons, Nature 477, 435 (2011).
- [10] R. McNeil, M. Kataoka, C. Ford, C. Barnes, D. Anderson, G. Jones, I. Farrer, and D. Ritchie, On-demand single-electron transfer between distant quantum dots, Nature 477, 439 (2011).
- [11] F. K. Malinowski, F. Martins, T. B. Smith, S. D. Bartlett, A. C. Doherty, P. D. Nissen, S. Fallahi, G. C. Gardner, M. J. Manfra, C. M. Marcus, *et al.*, Fast spin exchange across a multielectron mediator, Nat. Commun. 10, 1 (2019).
- [12] X. Mi, M. Benito, S. Putz, D. M. Zajac, J. M. Taylor, G. Burkard, and J. R. Petta, A coherent spin-photon interface in silicon, Nature 555, 599 (2018).
- [13] N. Samkharadze, G. Zheng, N. Kalhor, D. Brousse, A. Sammak, U. Mendes, A. Blais, G. Scappucci, and L. Vandersypen, Strong spin-photon coupling in silicon, Science 359, 1123 (2018).
- [14] A. J. Landig, J. V. Koski, P. Scarlino, U. Mendes, A. Blais, C. Reichl, W. Wegscheider, A. Wallraff, K. Ensslin, and T. Ihn, Coherent spin-photon coupling using a resonant exchange qubit, Nature 560, 179 (2018).
- [15] F. Borjans, X. Croot, X. Mi, M. Gullans, and J. Petta, Resonant microwave-mediated interactions between distant electron spins, Nature 577, 195 (2020).
- [16] F. Borjans, X. Croot, S. Putz, X. Mi, S. Quinn, A. Pan, J. Kerckhoff, E. Pritchett, C. Jackson, L. Edge, *et al.*, Split-gate cavity coupler for silicon circuit quantum electrodynamics, Appl. Phys. Lett. 116, 234001 (2020).

- [17] P. Harvey-Collard, J. Dijkema, G. Zheng, A. Sammak, G. Scappucci, and L. M. Vandersypen, Coherent spin-spin coupling mediated by virtual microwave photons, Phys. Rev. X. 12, 021026 (2022).
- [18] A. Stockklauser, P. Scarlino, J. V. Koski, S. Gasparinetti, C. K. Andersen, C. Reichl, W. Wegscheider, T. Ihn, K. Ensslin, and A. Wallraff, Strong coupling cavity QED with gate-defined double quantum dots enabled by a high impedance resonator, Phys. Rev. X. 7, 011030 (2017).
- [19] J. Zmuidzinas, Superconducting microresonators: Physics and applications, Annu. Rev. Condens. Matter Phys. 3, 169 (2012).
- [20] M. Tinkham, Introduction to superconductivity (Courier Corporation, 2004).
- [21] P. Harvey-Collard, G. Zheng, J. Dijkema, N. Samkharadze, A. Sammak, G. Scappucci, and L. M. Vandersypen, On-chip microwave filters for high-impedance resonators with gatedefined quantum dots, Phys. Rev. Appl. 14, 034025 (2020).
- [22] J. Bardeen, L. N. Cooper, and J. R. Schrieffer, Theory of superconductivity, Phys. Rev. 108, 1175 (1957).
- [23] S. Chockalingam, M. Chand, J. Jesudasan, V. Tripathi, and P. Raychaudhuri, Superconducting properties and Hall effect of epitaxial NbN thin films, Phys. Rev. B 77, 214503 (2008).
- [24] D. Hazra, N. Tsavdaris, S. Jebari, A. Grimm, F. Blanchet, F. Mercier, E. Blanquet, C. Chapelier, and M. Hofheinz, Superconducting properties of very high quality NbN thin films grown by high temperature chemical vapor deposition, Supercond. Sci. Technol. 29, 105011 (2016).
- [25] M. Shibalov, A. Mumlyakov, I. Trofimov, E. Timofeeva, A. Sirotina, E. Pershina, A. Tagachenkov, Y. Anufriev, E. Zenova, N. Porokhov, et al., Multistep atomic layer deposition process for ultrathin superconducting NbN films with high critical current density on amorphous substrate, Supercond. Sci. Technol. 34, 085016 (2021).
- [26] Y. Ivry, C.-S. Kim, A. E. Dane, D. De Fazio, A. N. McCaughan, K. A. Sunter, Q. Zhao, and K. K. Berggren, Universal scaling of the critical temperature for thin films near the superconductingto-insulating transition, Phys. Rev. B 90, 214515 (2014).
- [27] M. Faverzani, E. Ferri, A. Giachero, C. Giordano, B. Margesin, R. Mezzena, A. Nucciotti, and A. Puiu, Characterization of the low temperature behavior of thin titanium/titanium nitride multilayer films, Supercond. Sci. Technol. 33, 045009 (2020).
- [28] K. R. Amin, C. Ladner, G. Jourdan, S. Hentz, N. Roch, and J. Renard, Loss mechanisms in TiN high impedance superconducting microwave circuits, Appl. Phys. Lett. 120, 164001 (2022).
- [29] K. Yoshida, K. Watanabe, T. Kisu, and K. Enpuku, Evaluation of magnetic penetration depth and surface resistance of superconducting thin films using coplanar waveguides, IEEE Trans. Appl. Supercond. 5, 1979 (1995).
- [30] D. I. Schuster, Circuit quantum electrodynamics, Ph. D. Thesis (2007).
- [31] X. Mi, Circuit quantum electrodynamics with silicon charge and spin qubits, Ph. D. Thesis (2018).
- [32] K. D. Petersson, L. W. McFaul, M. D. Schroer, M. Jung, J. M. Taylor, A. A. Houck, and J. R. Petta, Circuit quantum electro-dynamics with a spin qubit, Nature 490, 380 (2012).
- [33] X. Mi, J. Cady, D. Zajac, J. Stehlik, L. Edge, and J. R. Petta, Circuit quantum electrodynamics architecture for gate-defined quantum dots in silicon, Appl. Phys. Lett. 110, 043502 (2017).